JGR

RESEARCH ARTICLE

Correspondence to:
F. Shi,
Feng.Shi@unh.edu

Foreshock wave interaction with the magnetopause: Signatures of mode conversion

Feng Shi[1], **Lei Cheng[2]**, **Yu Lin[2]**, and **Xueyi Wang[2]**

[1] Space Science Center, University of New Hampshire, Durham, New Hampshire, USA, [2] Department of Physics, Auburn University, Auburn, Alabama, USA

Abstract Our previous hybrid simulation (Shi et al., 2013) under a radial interplanetary magnetic field (IMF) and a supercritical solar wind Mach number has shown that foreshock compressional waves originated from the quasi-parallel (Q-∥) shock are mode converted to kinetic Alfvén waves (KAWs) at the Alfvén resonance surface of the subsolar magnetopause. In this paper, three-dimensional global dayside mode conversion is investigated for cases under various solar wind conditions using the global hybrid model. The global patterns and propagations of KAWs are distinguished and presented. Under a near-critical Mach number ($M_A = 3$), KAW structures due to mode conversion exhibit a feature of broader excitation regions in the magnetopause boundary layer (MPBL) compared to supercritical Mach number ($M_A = 5$) shocks. For cases with an oblique IMF with supercritical Mach numbers ($M_A = 5$), the amplitude of magnetosheath compressional waves is larger at the quasi-parallel shock (Q-∥) than at the quasi-perpendicular (Q-⊥) shock. Downstream of the Q-∥ shock, there is a general trend that the perturbations of density (N) and magnetic field (B) change from predominantly in-phase in the magnetosheath to antiphase near the MPBL. While downstream of the Q-⊥ shock, an antiphase relation between N and B is dominant throughout the magnetosheath and magnetopause except near the shock transition. The compressional drivers are found to reach an extended region of the magnetopause due to the combined effects of wave propagation in the plasma frame and flow convection, leading to a broad region of mode conversion at the magnetopause. Subsequently, the resulting KAWs can be carried to the regions downstream of the Q-⊥ shock owing to the flow convection at the magnetopause. The KAWs propagate poleward along the geomagnetic field lines and meanwhile are carried tailward by the ambient flows, and they are more intense in the downstream of Q-∥ shocks than downstream of Q-⊥ shocks.

1. Introduction

Magnetopause boundary layer (MPBL) has been known as the separation layer of the solar wind and magnetosphere and plays significant roles in the magnetospheric physics due to the occurrence of various transport processes involving mass, momentum, and energy from outside into the magnetosphere. It has been suggested that geomagnetic reconnection leads to the most direct transport process at the "open" magnetopause boundary with the southward interplanetary magnetic field (IMF) [*Russell and Elphic*, 1978, 1979; *Phan and Paschmann*, 1996; *Fuselier et al.*, 2000; *Hasegawa et al.*, 2002]. On the other hand, in the absence of reconnection at the "closed" magnetopause boundary during periods of northward IMF, the existence of efficient transport across MPBL has been reported [*Fujimoto et al.*, 1998; *Phan et al.*, 2000; *Hasegawa et al.*, 2003; *Wing and Johnson*, 2009]. In this scenario, plasma entries into the magnetosphere can result from wave-particle diffusive processes at the magnetopause boundary, where large-amplitude ultralow frequency waves are abundant and frequently observed [*Tsurutani and Thorne*, 1982; *Anderson et al.*, 1982; *Rezeau et al.*, 1989; *Chaston et al.*, 2008].

One of the most unique spectral features through the MPBL is the abrupt transition in wave polarization from compressional wave mode, frequently arising from the quasi-parallel (Q-∥) bow shock, to transverse mode [*Johnson and Cheng*, 1997]. Due to the magnetic field geometry of the Q-∥ shock, ultralow frequency (ULF) waves, turbulence, diamagnetic cavities, and bubbles are intrinsic features of the foreshock region [*Gosling et al.*, 1982; *Wibberenz et al.*, 1985; *Sibeck et al.*, 1989; *Fairfield et al.*, 1990; *Eastwood et al.*, 2005; *Kajdic et al.*, 2013; *Turner et al.*, 2013]. The abrupt changes in the wave polarization at the magnetopause have been observed in spacecraft explorations [*Johnson et al.*, 2001] and justify the existence of mode conversion from the

compressional to Alfvén modes, which provides a rich source of Alfvén waves at the magnetopause [*Chaston et al.*, 2008]. Multisatellite measurements of MPBL crossing also substantiate the suggestion of the mode conversion process and the presence of kinetic Alfvén waves (KAWs) at the magnetopause [*Chaston et al.*, 2007, 2008; *Yao et al.*, 2011]. It has been shown that the transverse electric and magnetic field components are well correlated with each other and match with small-scale KAW dispersion relations [*Stasiewicz et al.*, 2001; *Chaston et al.*, 2005].

KAWs can generate the parallel electric field $E_\parallel$, which combining with the perpendicular electric field can lead to effective heating and transport for particles on scales of the order of ion gyroradius. On such scales, the ion motion decouples from the magnetic field lines due to the finite perpendicular wavelength effects [*Johnson and Cheng*, 1997]. The dispersion relation of KAWs can be expressed as $\omega = k_\parallel V_A \sqrt{1 + k_\perp^2 (\rho_s^2 + \rho_i^2)}$, which gives the field polarization relation $\left|\delta E_\perp / \delta B_\perp\right| \simeq V_A \sqrt{1 + k_\perp^2 \rho_i^2}$ if $T_e/T_i \ll 1$, where $\rho_s = (T_e/m_i)^{1/2}/\Omega_i$, $\rho_i = (T_i/m_i)^{1/2}/\Omega_i$, Ω_i is the ion cyclotron frequency, and T_e and T_i are the electron and ion temperatures [*Johnson et al.*, 2001]. The dispersion relation of KAWs under broader conditions can be found in *Bellan* [2012].

Previous two-dimensional (2-D)/three-dimensional (3-D) hybrid simulations of mode conversion in simple current sheet geometries have shown the fundamental prospects both linearly and nonlinearly [*Lin et al.*, 2010, 2012]. With a pure single fast-mode compressional waves incident on the magnetopause current layer, the short wavelength KAWs are excited near the Alfvén resonance surface. Nonlinear effects in this process, such as generation of harmonics of the driver frequency and excitation of azimuthal KAW modes, are also observed. The simulation of *Lin et al.* [2012] demonstrates the crucial importance of 3-D physics in mode conversion.

Using a 3-D global hybrid model, interaction between the foreshock ULF waves/diamagnetic cavities and the dayside magnetosphere as well as the ion energization has been investigated [*Lin and Wang*, 2005; *Lin et al.*, 2007; *Wang et al.*, 2009]. In a recent 3-D global-scale hybrid simulation, *Shi et al.* [2013] identified KAWs from mode conversion associated with foreshock waves globally at the dayside magnetopause under a radial IMF (only B_x in IMF). It is also found that the evolution of the predominant KAWs with $k_x \rho_i \sim 1$ leads to the generation of KAWs dominated by the azimuthal wave numbers k_y, consistent with *Lin et al.* [2012] for mode conversion in the slab geometries. The resulting KAWs are found to decay into the magnetosphere from the Alfvén resonance surface $\omega \simeq k_\parallel V_A$, and these KAW perturbations, carrying the electromagnetic energy along the field lines, propagate poleward into the cusps along the MPBL.

Although such kinetic simulations have been carried out, previous simulation only studied a special case with a radial IMF and $M_A = 5$ for the solar wind [*Shi et al.*, 2013], and therefore, the global patterns and propagations of the KAWs from mode conversion process under more general IMF and solar wind conditions have not yet been reported. In general, the IMF usually has B_y and B_z components as well, "shifting" the Q-∥ region away from the subsolar region compared with the radial IMF case, and thus may modify the mode conversion process around the MPBL. Besides the IMF direction, the collisionless shocks associated with the case of $M_A \simeq 2-3$ are conventionally termed as "subcritical" shocks [*Tsurutani and Stone*, 1985], not only because the downstream of the subcritical shocks are distinct from the ones of higher Mach number "supercritical" shocks but because the patterns of the magnetopause may be quite different from those at higher Mach numbers [*Thomsen et al.*, 1993; *Farris et al.*, 1994]. To study such important nature of mode conversion and see how these key solar wind parameters control this process, in this paper we perform hybrid simulations under various solar wind conditions to examine the propagation and evolution of KAW structures from mode conversion in detail, including the downstream of both Q-∥ and quasi-perpendicular (Q-⊥) shocks.

This paper is a continued study from *Shi et al.* [2013], and the purpose of it is to investigate how the key parameters of the IMF and solar wind influence the mode conversion process in the MPBL. Three typical cases with a radial or northward IMF are presented, as listed in Table 1. In Case 1, a very low solar wind Mach number ($M_A = 3$) with radial IMF is used to study mode conversion under near-critical shock cases. The sign of IMF B_y in Case 2 is consistent with the Parker spiral configuration, whereas for Case 3 B_y has an opposite sign and B_z exists in order to see a broader influence of IMF components. In our spherical coordinate Geocentric Solar Magnetospheric (GSM) system, θ is the pitch angle (between the positive z axis and the line from the origin to the point), and ϕ is the azimuthal angle with respect to the Sun-Earth line in x-y plane (between the positive x axis and the projection in x-y plane from the origin to the point). The outline of this paper is as follows. The simulation model is described in section 2. The simulation results are presented in section 3. A concluding summary is given in section 4.

Table 1. Brief Case Description: Initial IMF and Solar Wind Plasma Conditions[a]

Case Description	θ	ϕ	B_x	B_y	B_z	M_A
Case of Shi et al.[b]	90°	180°	$-1.0\,B_0$	0	0	5
Case 1	90°	180°	$-1.0\,B_0$	0	0	3
Case 2	90°	150°	$-0.866\,B_0$	$0.5\,B_0$	0	5
Case 3	70°	240°	$-0.470\,B_0$	$-0.814\,B_0$	$0.342\,B_0$	5

[a]IMF, interplanetary magnetic field.
[b]Refer to *Shi et al.* [2013].

2. Simulation Model

The dayside global-scale hybrid simulation scheme in this work was developed by *Swift* [1996] and described by *Shi et al.* [2013]. In this model, ions are treated as fully kinetic particles, while electrons as a massless fluid. Specifically, the ions are advanced by their equation of motion, the electric field is determined by the electron momentum equation, and the magnetic field is updated by Faradays's law. The more detailed description of the model can be found in *Shi et al.* [2013].

2.1. Simulation Setup

In the following presentation, spherical coordinates are used in the GSM system. The magnetic field $\boldsymbol{B}$ is scaled by the IMF $\boldsymbol{B}_0$; the ion number density N by the solar wind density N_0; the time t by the inverse of the solar wind ion gyrofrequency, Ω_{i0}^{-1}; the plasma flow velocity $\boldsymbol{V}$ by the solar wind Alfvén speed V_{A0}; the temperature by V_{A0}^2; and the length by the Earth radius R_E. The simulation domain contains the system of the bow shock, magnetosheath, and magnetosphere in the dayside region with GSM $x > 0$ and a geocentric distance $4\,R_E \leq r \lesssim 22\,R_E$. The Earth is located at the origin $(x, y, z) = (0, 0, 0)$. Outflow boundary conditions are utilized at $x = 0$, while inflow boundary conditions of the solar wind are applied at $r \simeq 22\,R_E$. The inner boundary at $r = 4\,R_E$ is assumed to be perfectly conducting, and an additional cold ion fluid is used to model the inner magnetosphere at $r \lesssim 7\,R_E$.

The ion inertial length in the solar wind is chosen as $d_{i0} = 0.1\,R_E$. A uniform solar wind plasma with ion beta value $\beta_i = 0.5$ is employed, flowing into the system along the $-x$ direction with an isotropic drifting Maxwellian distribution. A total of about 4×10^8 particles are utilized, and the number density of the macroion particles is set to be $N_0 = 11,000\,R_E^{-3}$ in the solar wind. An isothermal electron equation of state is assumed, with $\beta_e = 2.0$ in the solar wind plasma to ensure a temperature ratio $T_e/T_i \simeq 0.1\text{–}0.2$ at the magnetopause.

Nonuniform grids are exploited in the radial direction, with a higher resolution of $\Delta r = 0.05\,R_E$ at $\sim 8\text{–}13\,R_E$ throughout the magnetopause and the bow shock regions in order to identify the small-scale kinetic wave structures, while $\Delta r = 0.1\,R_E$ to $0.14\,R_E$ in the farther upstream solar wind regions. A total grid of $N_r \times N_\phi \times N_\theta = 180 \times 104 \times 130$ is used, with particle numbers per cell ranging from ~ 60 to 400 for the main simulation regions from the magnetopause to the upstream solar wind. The time step to advance the positions of particles is $0.05\,\Omega_{i0}^{-1}$.

2.2. Numerical Discussion

The grid resolution and particle number used for this work are chosen on the basis of physical and numerical requirements. As described above, we use a nonuniform curvilinear mesh with finest spatial resolution of $\Delta r = 0.5\,d_{i0}$ throughout the magnetopause, magnetosheath, and bow shock regions, where local d_i becomes the smallest. Note that hybrid models can resolve ion kinetic scales up to $k\rho_i \sim 1$ (wavelength $\lambda \sim 6\rho_i$), which means the grid sizes used here are small enough to resolve the waves in the foreshock, where the ion Larmor radius is determined by the shock heated ions, as well as the magnetopause waves. Correspondingly, hybrid models are valid for low-frequency physics up to $\omega \sim \Omega_i$. The finite ion gyroradius effects are resolved with time steps much smaller than the gyroperiod ($\Delta t = 0.05\Omega_i$ in our simulations). Moreover, the local hybrid simulations by *Lin et al.* [2010] taking use of a finer grid resolution have shown that the maximum wave energy of mode conversion appears at the longer wavelength, $k_\perp \rho_i \sim 0.4$, which is well resolved by our global simulations.

Other global hybrid simulations [e.g., *Lin and Wang*, 2005; *Blanco-Cano et al.*, 2009; *Karimabadi et al.*, 2014] have been performed with similar spatial and temporal resolutions. For instance, *Karimabadi et al.* [2014] carried out 2-D global hybrid simulations in a Cartesian coordinate system, using spatial resolution of $0.25\text{–}1\,d_{i0}$

and particle numbers per cell up to 200, which is found to be enough to resolve the ion kinetic effects. A comparison of spatial and temporal resolutions and particle numbers used in various hybrid and particle-in-cell simulations can be found in Table 1 from *Yang et al.* [2016]. We have checked the effects of the number of particles per cell by doubling and quadrupling the number and also performed runs of higher spatial resolution by doubling the grid spacing and particle number simultaneously. The results are found to be similar to those shown in this paper, indicating a good convergence of calculation.

It is also worth noting that the nonuniform curvilinear coordinate lines used in our simulation have the advantage of catching and resolving the bow shock and the magnetopause structure better than that of the Cartesian coordinates since the radial coordinate lines are nearly along the gradient of the boundary layers of concern. This also saves the computation resource by using denser grids to the specific direction and regions.

3. Simulation Results

As mentioned before, the purpose of this paper is to find out the influence of the key solar wind parameters on the mode conversion in geo-space. To understand the role played by each of these factors, it is necessary to compare the results with a different parameter in *Shi et al.* [2013] while keeping other parameters the same. Therefore, we begin by examining Case 1 with $M_A = 3$, which is similar to that presented in *Shi et al.* [2013] with a radial IMF but $M_A = 5$. The comparison of IMF components will be given in the following subsections.

3.1. Identification of Mode Conversion With $M_A = 3$

The 3-D structures of B with typical field lines and N at $t = 80$ in logarithmic scales for Case 1, as well as B and N in a similar case with radial IMF but $M_A = 5$ in *Shi et al.* [2013], are shown in Figure 1. Note that a much larger domain than that of *Shi et al.* [2013] is presented in order to show the foreshock region. For Case 1, the Q-∥ shock is around the subsolar region, and the bow shock is seen at a standoff distance of $x \sim 13.5\,R_E$, across which earthward B and N increase dramatically. In the upstream of the Q-⊥ shock ($|y| > 15\,R_E$ and $|z| > 15\,R_E$), the field lines are almost unperturbed, and there are negligible perturbations in B and N. Foreshock waves, on the other hand, can be clearly seen from the wavy field lines in the upstream of the Q-∥ shock. Similar to $M_A = 5$ case, foreshock cavities with decreased magnetic field and density are seen in the turbulent Q-∥ foreshock region, and they are identified as whistler-type electromagnetic waves due to the nonlinear interaction between the backstream ion beams and the solar wind plasma [*Lin*, 2003; *Wang and Lin*, 2003], with wave vectors nearly parallel to the magnetic field lines [*Lin and Wang*, 2005]. It also shows the fine turbulent structures downstream of the Q-∥ shock in the magnetosheath with waggling field lines and perturbations in B and N. The magnetosheath is thicker than those in the case of $M_A = 5$ [*Shi et al.*, 2013]. In addition, much weaker magnetic pulses and lower plasma density in the magnetosheath ($\sim$50%) can also be seen for Case 1 and so does the solar wind dynamic pressure. Across the magnetopause which divides the Earth's magnetosphere from the outer space, B increases but N decreases sharply due to the total pressure balance. Note that in this case with a radial IMF reconnection occurs at $z \lesssim -7\,R_E$ in the Southern Hemisphere where the convection is southward and strong. Therefore, reconnection structures do not affect the subsolar region and the results we discuss thereafter. The location of the dayside reconnection in the midlatitude to high latitude under a radial IMF is also consistent with global MHD simulations [*Tang et al.*, 2013] and satellite observations [*Pi et al.*, 2017]. Figure 2 shows the time sequence of various quantities along the Sun-Earth line $x = 9 - 20\,R_E$ from $t = 40 - 150$. The oscillating MPBL and the near-critical Mach number Q-∥ shock can be recognized around $x \sim 10\,R_E$ and $x \sim 13\,R_E$, respectively. The typical foreshock waves upstream of the Q-∥ shock are marked at $t \sim 45 - 60$ from $x \sim 17 - 14\,R_E$, and the typical compressional wave packets propagate from the bow shock at $t \sim 40$ to the MPBL at $t \sim 90$. From the slope of the wave structures, it can be seen that the propagation of foreshock waves with a speed of $\sim 2V_{A0}$ in the simulation frame of reference, generated in the upstream of Q-∥ with in-phase relation between B and N propagates earthward, slows down in the magnetosheath to the speed of $\sim 0.6V_{A0}$ in the simulation frame and finally impinges onto the magnetopause. In addition, there are also waves at the shock front reflected back into the upstream region, as seen in $E_\parallel$ and $J_\parallel$ perturbations. Note that when the series of wave packets interact with the magnetopause, strong perturbations in the parallel electric field $E_\parallel$ are excited near and inside (shown in circled regions) the MPBL transition, from $t \simeq 40$ to 60 and 70 to 90. These excited waves are dominated with short wavelengths of $k_x \rho_i \sim 0.5 - 1$. Meanwhile, perturbations in the well-correlated parallel current $J_\parallel$ are also evident near the magnetopause region, indicating signatures of KAWs identified by *Shi et al.* [2013].
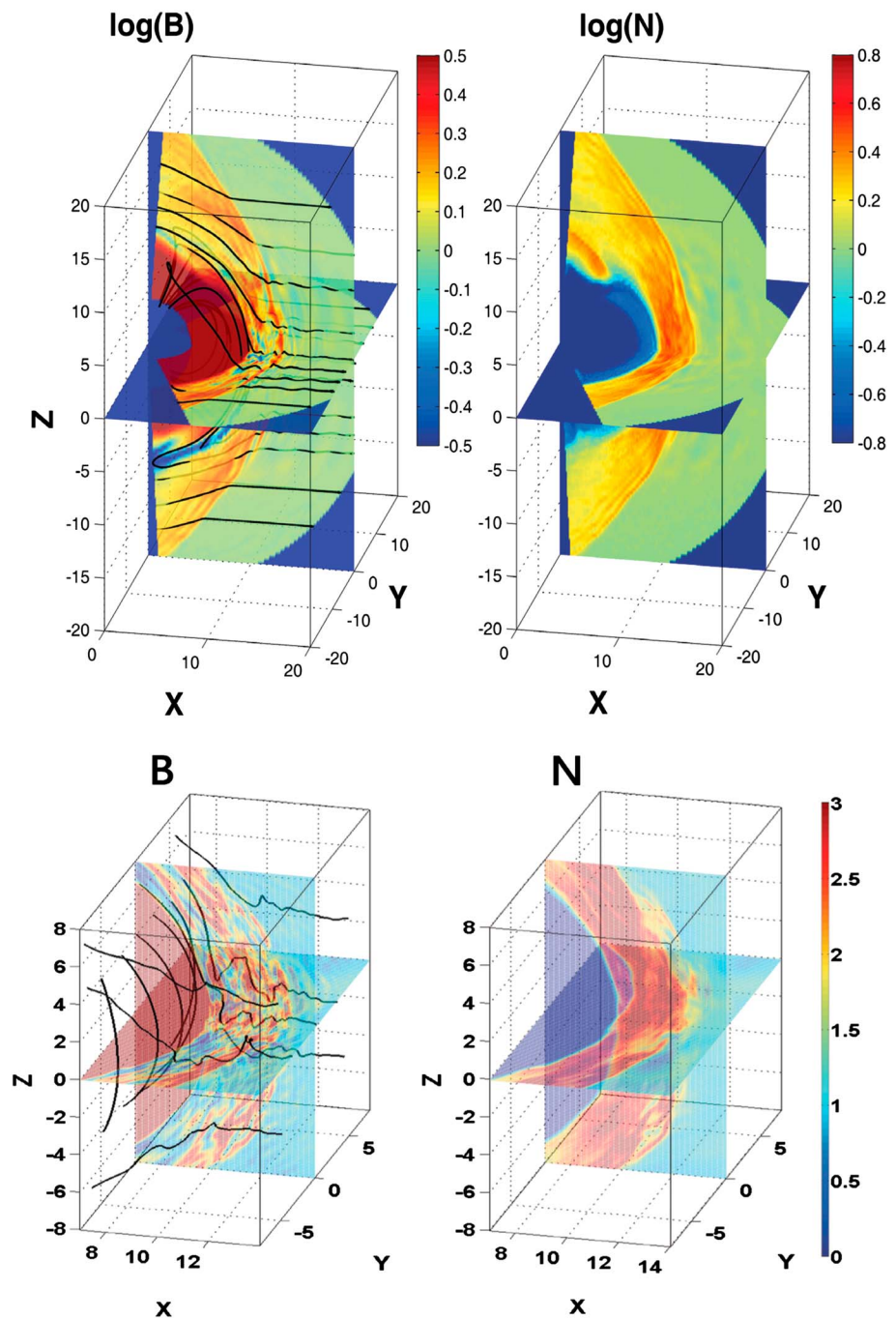
Figure 1. (top) Spatial contours of geomagnetic field strength B and ion density N at $t = 80$ in logarithmic scales showing the 3-D structures of self-consistently generated bow shock and magnetopause, with radial IMF and $M_A = 3$ (Case 1 in Table 1). (bottom) B and N at $t = 150$ with radial IMF but $M_A = 5$ [Shi et al., 2013]. Typical field lines are shown in the magnetic field plots. Note that in order to show the foreshock region, the domain (Figure 1, top) larger than that of Shi et al. [2013] (Figure 1, bottom) is presented.

In addition, the lower convection flow speed leads to a smaller dynamic pressure and thus a smaller compression of the magnetopause. Figure 3 shows the spatial cuts of B, N, B_y, $E_\parallel$, and $J_\parallel$ through the MPBL region along the Sun-Earth line at $t = 93$. Compared with Figure 6 in Shi et al. [2013] for $M_A = 5$, one can see a much broader MPBL, in which B increases and N decreases earthward, with a thickness of $\sim 1\ R_E$ for the small Mach number $M_A = 3$ case. For $M_A = 3$, solar wind dynamic pressure is much weaker so that the magnetopause is less compressed and become broader due to the pressure balance. Note that the mode conversion layer also
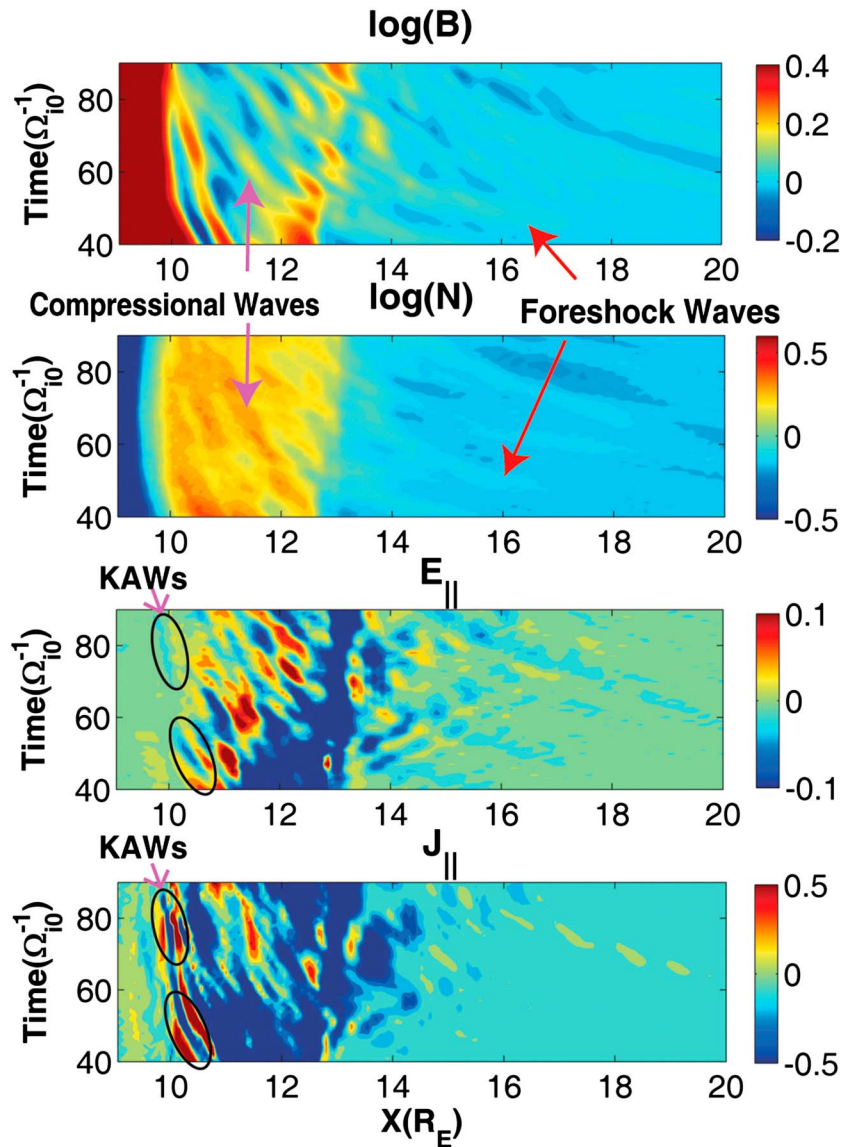
Figure 2. Time evolution of spatial profiles of $\log(B)$, $\log(N)$, $E_\parallel$, and $J_\parallel$ along the Sun-Earth line $x = 9\,R_E - 20\,R_E$ during the time interval $t = 40-90$ for Case 1. Typical compressional waves propagating toward the MPBL and foreshock waves are marked, and KAWs aroused around the MPBL are shown in circles.

looks broader (as seen from smoother change of B and N in the transition layer) maybe because the resonance points are distributed more broadly in the broadened MPBL. The corresponding local Alfvén speed V_A in the MPBL is also smaller and increases approximately from $\sim 0.5V_{A0}$ to $\sim 6V_{A0}$. Although weaker in the broadened MPBL, waves with $E_\parallel$ are strongly enhanced near $x \simeq 10.5\,R_E$. The excited waves radiate back to the magnetosheath side, and the excited wave pattern shows a decay spatial profile on the magnetospheric side. Similar behaviors are seen in $J_\parallel$ and B_y. The correlation of these quantities are consistent with the KAW structures dominated by k_x in the analytical theory [*Hasegawa and Chen*, 1976] and previous hybrid simulations of mode conversion for a local magnetopause [*Lin et al.*, 2010, 2012; *Shi et al.*, 2013]. Around $x \simeq 9.8-10.6\,R_E$ on the magnetospheric side, however, a series of short wavelength structures of excited waves can be perceived in Figure 3, which is different from higher Mach number case where such laminar k_x modes are not observed. Due to the larger and slower oscillations of the MPBL, as well as the nonmonotonic magnetosonic and whistler waves downstream of the shock ramp [*Omidi et al.*, 1990; *Thomsen et al.*, 1993], the mode conversion point with near-critical shocks could change more dramatically over time and space than the one with supercritical shocks, which may be the reason that the waves are so wide into the left side of the mode conversion point at this moment. The parallel wavelength ($k_\parallel$) of incoming waves from the magnetosheath and the local ion
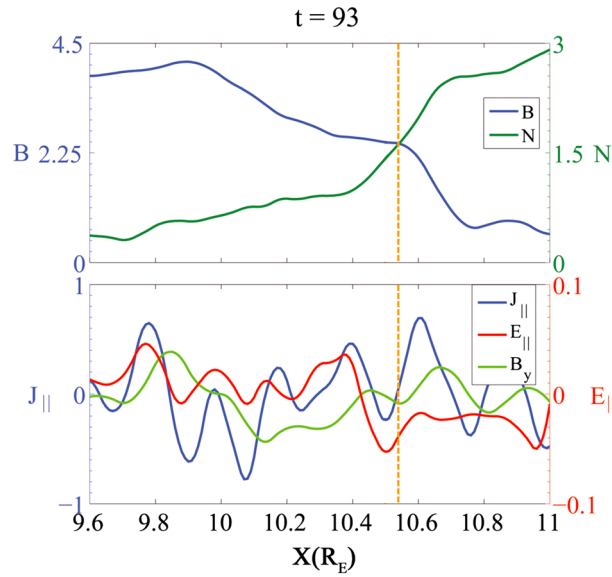
Figure 3. Spatial cuts of various quantities through the MPBL along the Sun-Earth line at $t = 93$ for Case 1. The vertical dashed lines mark the averaged resonance point.

Larmor radius (ρ_{i0}) is measured $\sim 3-8\ R_E$ and $\sim 0.5d_{i0}$, leading to $k_\parallel \rho_i \sim 0.04-0.1$. Meanwhile, the perpendicular wavelength in x direction (k_x) is $\sim 0.2-0.5\ R_E$, corresponding to $k_x \rho_i \sim 0.5-1$, and the dominant incident wave frequency is estimated $\sim 0.3\Omega_{i0}$ along with the ion gyrofreqency $\Omega_i \sim 2-3\Omega_{i0}$ at the magnetopause. The Alfvén resonance condition $\omega = k_\parallel V_A(1 - \omega^2/\Omega_i^2) \sim k_\parallel V_A$ thereby on average requires $V_A \sim 2V_{A0}$, which corresponds to $x \sim 10.55\ R_E$ in the MPBL and is indicated by the yellow dashed vertical line in Figure 3.

When a background magnetic field is pointing in the $+z$ direction and a KAW with the wave vector $\boldsymbol{k}$ in the x-z plane, as seen above for the mode structures along the normal of the subsolar MPBL, the wave polarizations in Alfvén waves with $k_\perp = k_x$ are dominant perturbations by B_y and E_x. From the kinetic theory for the KAW, $\delta E_x = V_A \delta B_y \left\{ 1 + T_e/T_i \left[1 - I_0\left(\lambda_i\right) e^{-\lambda_i} \right] \right\}$ where $\lambda_i = k_x^2 \rho_i^2$ and $I_0\left(\lambda_i\right)$ is the modified Bessel function of the first kind, with $k_x \rho_i \sim 0.5-1$ and $T_e/T_i \sim 0.2$ at the magnetopause, the relation $\delta E_x \simeq \sqrt{1 + k_\perp^2 \rho_i^2}\, V_A \delta B_y \simeq 1.1 V_A B_y$ still holds based on the Pade approximation compared with the supercritical shock case *Shi et al.* [2013]. The polarization relation of the waves with locally enhanced $E_\parallel$ marked by circles in equatorial and noon-meridian planes is shown in Figure 4 at $t = 89$. Consistent with the theoretical prediction for KAWs, the waves in the MPBL are found to be dominated by δB_y and δE_x. Figure 4 shows δE_x versus δB_y for enhanced $E_\parallel$ points inside the circles, with the violet dashed lines denoting the polarization relation $E_x = 1.1 V_A \delta B_y$ for KAWs. δB_y and δE_x are defined relative to "equilibria," which are calculated from the average fields over data time duration after $t = 40$. Here V_A is the local Alfvén speed based on the equilibrium B and N. It is seen from Figure 4 (right column) that the Alfvén-mode polarization relation is nearly satisfied. Note that the signs of the slope of the violet lines in Figure 4 (right column) represent the direction of the Alfvén-mode propagation along z, which is nearly the direction of the magnetic field lines. Concretely, for Figure 4 (bottom row), the wave structures in the MPBL obtained from the simulation consist of two parts: the positive slope for $z > 0$, indicating a wave branch traveling northward along the field lines, and the negative slope for $z < 0$, denoting another branch propagating southward along the field lines. Similar to the diagnostics in *Shi et al.* [2013], these waves are identified as KAWs that are mode converted from the compressional waves interacting with the magnetopause.

3.2. Mode Conversion and Generation of KAWs in the Supercritical Shock Case With Only IMF B_x and B_y

We now examine Case 2 with a supercritical Mach number $M_A = 5$, similar to the case discussed in *Shi et al.* [2013], but with an oblique IMF. The IMF is assumed to be in the x-y plane with $B_z = 0$, and the field makes a 30° angle relative to the x axis. Spatial contours of the magnetic field B with typical geo-space field lines and ion density N at $t = 120$ obtained in Case 2, in the noon meridian and equatorial planes, are shown in Figure 5. The self-generated bow shock and the magnetopause can be recognized at standoff distances around $12\ R_E$ and $10\ R_E$, respectively, as seen from the B and N contours. In this case with an oblique IMF, Figure 5 shows a thicker magnetosheath on the $y > 0$ side and a wider foreshock region with wave turbulence on the $y < 0$ side, rather than being symmetric about the subsolar region. The Q-∥ shock regions are "shifted" to the dawnside on the bow shock in the equatorial plane, centered around $y \simeq -3\ R_E$. Note that such asymmetric bow shock from dawn to dusk can be caused by both MHD and kinetic effects. In our simulations, deflected flows similar to *Nishino et al.* [2008] that are responsible for the dawn-dusk asymmetry due to MHD effect are observed (shown in Figure 7). Meanwhile, the Q-∥ shock does not have a well-define shock front and contains an extended region of foreshock waves, which is due to the ion kinetic effect. As a result, the magnetosheath
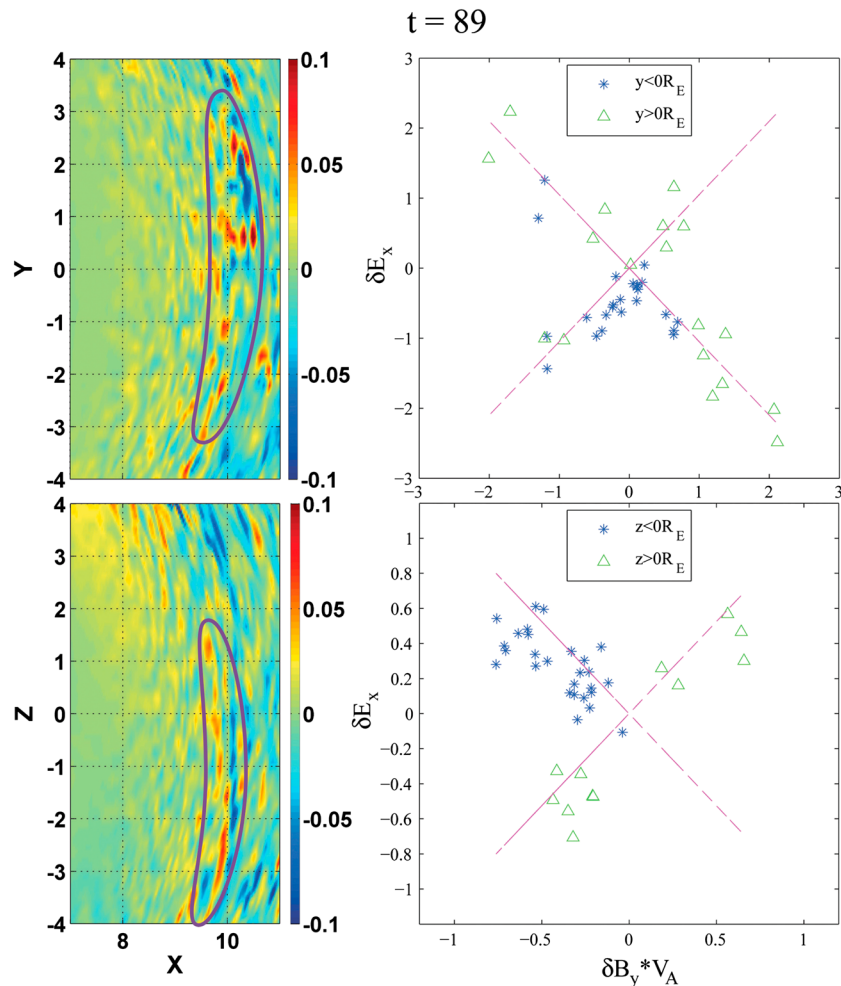
Figure 4. (top left) Spatial profile of $E_{\parallel}$ around the MPBL in the equatorial plane at $t = 89$ for Case 1. (top right) Corresponding polarization relation in the circled regions in Figure 4 (top left) showing Alfvén modes propagating in different directions along the field lines. (bottom left) Spatial profile of $E_{\parallel}$ around the MPBL in the noon-meridian plane at $t = 89$ for Case 1. (bottom right) Corresponding polarization relation in the circled regions in Figure 4 (bottom left) showing Alfvén modes. The violet dashed lines in Figure 4 (right column) represent the theoretically predicted polarization relation $\delta E_x = \pm 1.1 V_A \delta B_y$ for the KAWs.

on the dawnside appears much thinner than on the duskside. In addition, compressional pulses in B and N, as well as transverse magnetic field perturbations, are present in the magnetosheath. The wave perturbations are mainly due to the turbulence in the bow shock and foreshock region generated by backstreaming ions in the foreshock of the Q-$\parallel$ shock [*Lin and Wang*, 2005].

To see the dynamical propagation of the compressive wave structures at the bow shock, the spatial profiles of various quantities along the Sun-Earth line are drawn in Figure 6 in a time sequence of $t = 40–150$. From Figure 6 we see that the incoming compressive wave pulses [*Lin and Wang*, 2005; *Shi et al.*, 2013] characterized by the perturbations in B and N repeatedly propagate onto the magnetopause from the bow shock region along the Sun-Earth line. Moreover, along the Sun-Earth line, the magnetopause can be distinguished around 9.8 R_E from the abrupt increase in B and decrease in N earthward, and the bow shock is located roughly around 11.9 R_E. Compared with Figure 2 for Case 1, the earthward propagation speed of the waves is larger due to the larger convection speed and Mach number, and thus the "slope" of indicated compressional pulses is smaller. The stronger wave pulses also lead to stronger perturbations of $E_{\parallel}$ and $J_{\parallel}$ marked by circles in Figure 6. A typical case of these earthward propagating compressive waves is marked in Figure 6 at $t \simeq 70$ when a new packet of wave pulses are generated at the bow shock and carried by the convective solar wind plasma earthward to the MPBL at about $t = 90$. In this case, the typical Alfvén speed is about $1.7 V_{A0}$ in the magnetosheath outside
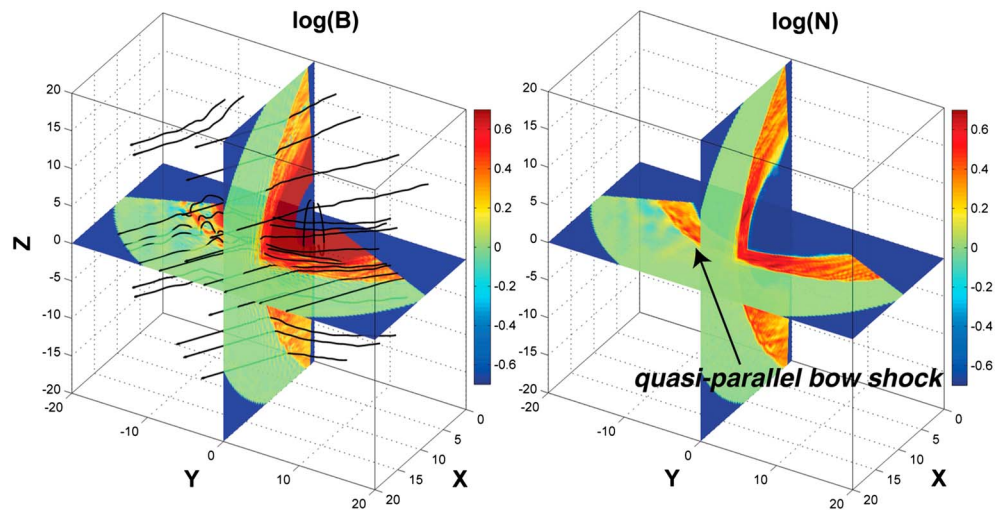
Figure 5. Spatial contours of the magnetic field B and ion density N at $t = 120$ (in logarithmic scales), for Case 2 with IMF B_x and B_y components in Table 1, showing the 3-D structures of self-consistently generated bow shock and magnetopause, as well as the compressive pulses in the magnetosheath. Typical field lines are also shown in the magnetic field plot.

the MPBL around 11 R_E, where the compressive waves propagate sunward with a speed about $2–3V_{A0}$ in the frame of convective plasma. And since the earthward and azimuthal plasma convection speed is about $5V_{A0}$, the net propagation speed of $\sim 2–3V_{A0}$ in the Earth frame of reference is seen. While approaching the magnetopause, the compressional wave pulses are slowing down significantly in the x direction and consequently impinging onto the magnetopause.
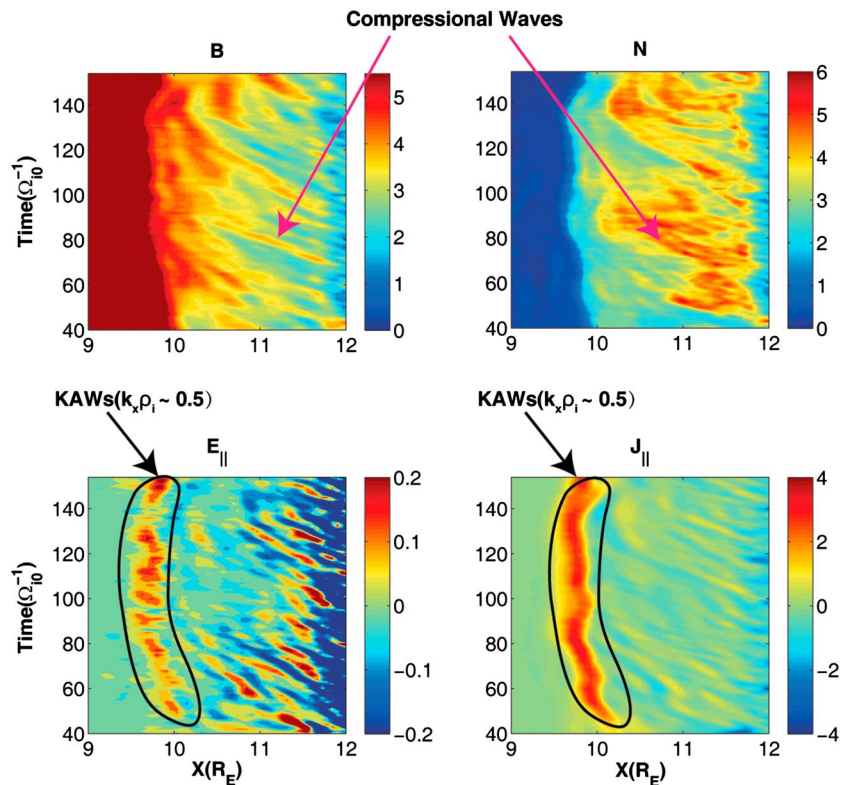

Figure 6. Time evolution of spatial profiles of various quantities along the Sun-Earth line during the time interval $t = 40–150$ for Case 2. Typical compressional waves are marked, and the circles highlight the areas of the KAW structures with locally excited $E_{\parallel}$ around the MPBL.

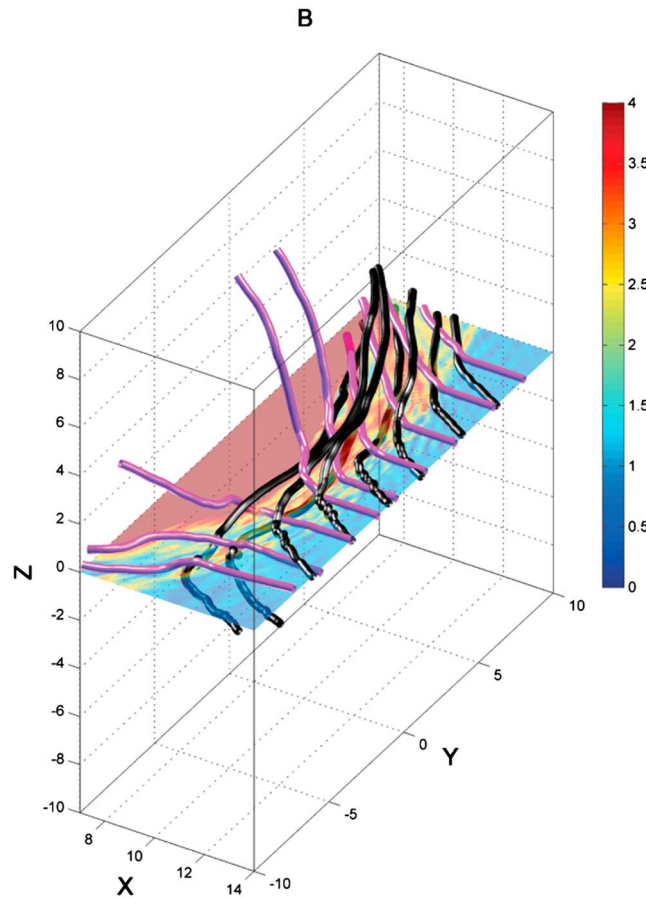**Figure 7.** Contours of magnetic field B in the equatorial plane at $t = 110$ for Case 2, showing the Q-∥ shock region around $y = 0 - (-6)\ R_E$. Typical 3-D magnetic field lines (black) and flow streamlines (purple) around the equatorial plane are also shown. Note that the convective flow is diverted dawn/dusk around $y = -3\ R_E$ at the magnetopause.

In this scenario, the mode conversion process is expected to be different from the radial IMF case, because the center of the Q-∥ region is shifted away from the subsolar point. Although the azimuthal convective flow speeds are more or less similar between the cases, the wave structures can be readily off the Sun-Earth line/plane due to the existence of B_y component locally. Due to the finite azimuthal convection away from the subsolar region, the interaction time between the incoming waves and the magnetopause could be dramatically reduced compared with radial IMF cases when the Mach numbers of the solar wind are quite similar. Therefore, it can be found that the $E_∥$ in the subsolar region has weaker intensity (~50%) in Case 2 than the radial IMF case [*Shi et al.*, 2013] with the same Mach number ($M_A = 5$), but it can still be seen that perturbations in $E_∥$ are excited locally around the subsolar transition layer after the wave pulses impact on the MPBL at $t \simeq 50-150$, as shown by the left bottom circle in Figure 6. These wave structures are examined predominantly to be of short wave lengths $k_x \rho_i \simeq 0.5-1$.

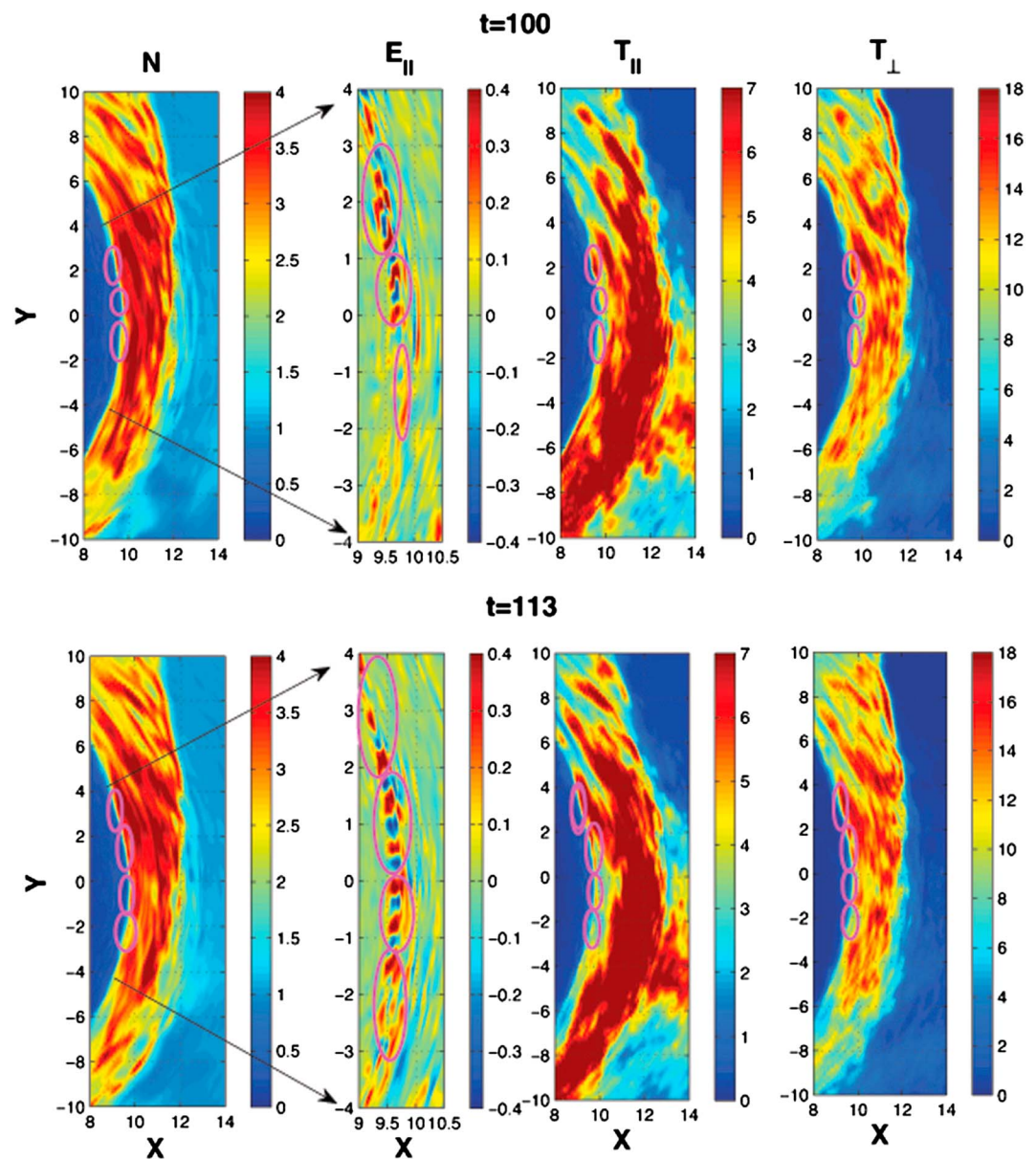Figure 7 shows typical 3-D magnetic field lines (black) and flow streamlines (purple) of Case 2 at $t = 110$. Spatial contours of B on the equatorial plane is also given, from which the magnetopause and bow shock can be distinguished. Short wavelength structures carried earthward by the convective plasma are seen in the magnetosheath, especially around the downstream of the Q-∥ bow shock, centered around $y \sim -3\ R_E$. Unlike the radial IMF cases, the smallest speed of azimuthal convective flow near the magnetopause is not around the subsolar region but located at $y \simeq -3\ R_E$ where flows are diverted to dawn for $y \lesssim -3\ R_E$ (or dusk for $y \gtrsim -3\ R_E$). Due to this azimuthal component change of the flow convection, waves resulting from the interaction at the magnetopause, downstream of the Q-∥ shock on the dawnside (e.g., around $y \sim -3\ R_E$), may be carried and propagate azimuthally to downstream of the Q-⊥ shock on the dawnside.

To illustrate the azimuthal distribution of the wave interaction, the left, third, and fourth columns of Figure 8 show the equatorial contours of density N, parallel ion temperature $T_∥$, and perpendicular ion temperature $T_⊥$ at $t = 100$ (top row) and $t = 113$ (bottom row), while the second column depicts the corresponding zoom-in structure of $E_∥$ around the magnetopause. At $t = 100$, significant $T_∥$ enhancements and density perturbations are seen in the foreshock of the Q-∥ shock due to the field-aligned ion beams. A temperature anisotropy with $T_∥ > T_⊥$ is seen both upstream and downstream of the shock on the dawnside. On the duskside, the upstream of the Q-⊥ shock is quiet, while a strong perpendicular heating leads to $T_⊥ > T_∥$ in the magnetosheath. As a result of the incoming foreshock waves that impinge on the magnetopause, as shown in Figure 6, perturbations are seen on the surface of the magnetopause. Some of these surface perturbation structures in N, $T_∥$, and $T_⊥$ are highlighted by the purple circles in Figure 8 (top row) for $t = 100$. These surface waves are in a broad region, not limited to the direct downstream of the Q-∥ shock, as discussed above on the basis of the flow convection pattern. Associated with the waves on the magnetopause are enhancements of $E_∥$, indicated

Figure 8. The equatorial contours of density N, parallel ion temperature $T_{\parallel}$, and perpendicular ion temperature $T_{\perp}$ at (top row) $t = 100$ and (bottom row) $t = 113$. The (second column) corresponding zoom-in view of $E_{\parallel}$ around the magnetopause, for Case 2. Some of the perturbations are highlighted by the purple circles.

by the corresponding purple circles. At $t = 113$, these surface waves have spread out around the magnetopause following the azimuthal convection, and more wave structures are present, as indicated by the purple circles in Figure 8 (bottom row).

Figure 9 examines the properties of compressional waves in the magnetosheath and the magnetopause, for both the Q-$\parallel$ and Q-$\perp$ shock sides. Shown in Figure 9 (top row) are the time variations of B and N at two distinct locations along $y = -6\,R_E$ in the equatorial plane, around the MPBL location $x = 8.7\,R_E$, and in the magnetosheath at $x = 10.3\,R_E$. Figure 9 (bottom row) shows the results at $y = 10\,R_E$, again in the magnetopause ($x = 5.2\,R_E$) and magnetosheath ($x = 8.6\,R_E$). At $y = -6\,R_E$ downstream of the Q-$\parallel$ shock, the magnetosheath waves are dominated by an in-phase relation between B and N, although they are also mixed with an antiphase relation. The large-amplitude oscillations are mainly due to the oscillations of the magnetopause. In the magnetopause ($x = 8.7\,R_E$), oscillations with an antiphase relation between B and N are present. It can also be concluded that the waves in MPBL are dominated by the antiphase relation of B and N, while those
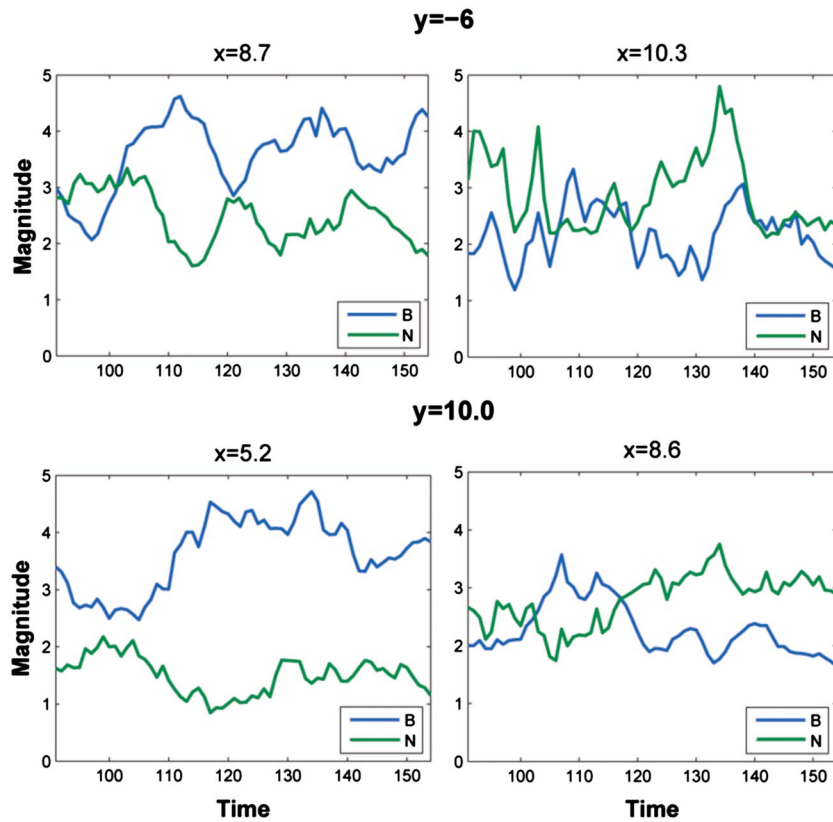
Figure 9. Time variations of *B* (blue) and *N* (green) at two distinct locations in the equatorial plane for Case 2. (top row) At $y = -6\,R_E$, around the MPBL location $x = 8.7\,R_E$, and in the magnetosheath at $x = 10.3\,R_E$. (bottom row) At $y = 10\,R_E$, again in the magnetopause $x = 5.2\,R_E$, and magnetosheath $x = 8.6\,R_E$.

in the magnetosheath region are dominated by the in-phase relation. This change of the wave polarization is similar to that in the case with IMF $B_y = 0$ discussed in *Shi et al.* [2013]. In the magnetopause ($x = 8.7\,R_E$), the time variations are mainly due to the low-frequency magnetopause surface waves, which include compressional surface perturbations and mode converted waves that will be identified later. At $y = 10\,R_E$ deep on the side of the Q-⊥ shock, the amplitude of the magnetosheath compressional waves is much smaller than those at $y = -6\,R_E$. These waves have the properties of mirror mode and Alfvén ion cyclotron waves [*Price et al.*, 1986; *Czaykowska et al.*, 1998; *Blanco-Cano et al.*, 2006], which have a predominant antiphase relation between *B* and *N*. At the magnetopause at $x = 5.2\,R_E$ on the Q-⊥ side, the *B* and *N* are seen to change with a much smaller frequency, and the change is mainly due to the oscillation of the global bow shock-magnetosphere system. To conclude, on the Q-∥ shock side, it is predominated by in-phase compressional waves in the magnetosheath and antiphase mode converted waves in the magnetopause, while on the Q-⊥ shock side, both in-phase compressional waves and antiphase mirror mode and Alfvén ion cyclotron mode waves are present in the magnetosheath, so the change of the phase relation is not as obvious as on the Q-∥ side.

The power spectra of perturbations δB and δN in the ω-x space at $y = -6\,R_E$ in the equatorial plane are shown in Figure 10 (left column, first and second panels), while the spectra of phase angle between δB and δN are shown in the bottom row. Corresponding results at $y = 10\,R_E$ are plotted in Figure 10 (right column). The perturbations are calculated with respect to the time-averaged values from $t = 91$ to 154. The average locations of the magnetopause and the bow shock are marked by MP and BS, respectively. It can be seen from Figure 10 that the wave power both around the bow shock and in the magnetosheath on the Q-∥ side ($y = -6\,R_E$) is much stronger than the power on the Q-⊥ side ($y = 10\,R_E$). The low-frequency global oscillations can be seen at both locations and on both *B* and *N*, around $\omega \sim 0.1\Omega_{i0}$, on the Q-∥ side at $y = 6\,R_E$, although there exist mixed phases for the incoming waves in the magnetosheath, the correlation between the density and magnetic field in the magnetosheath is overall consistent with [*Shi et al.*, 2013] as well as what we have discussed in Figure 9; the in-phase compressional waves are predominant and down deep into the magnetosheath. On the
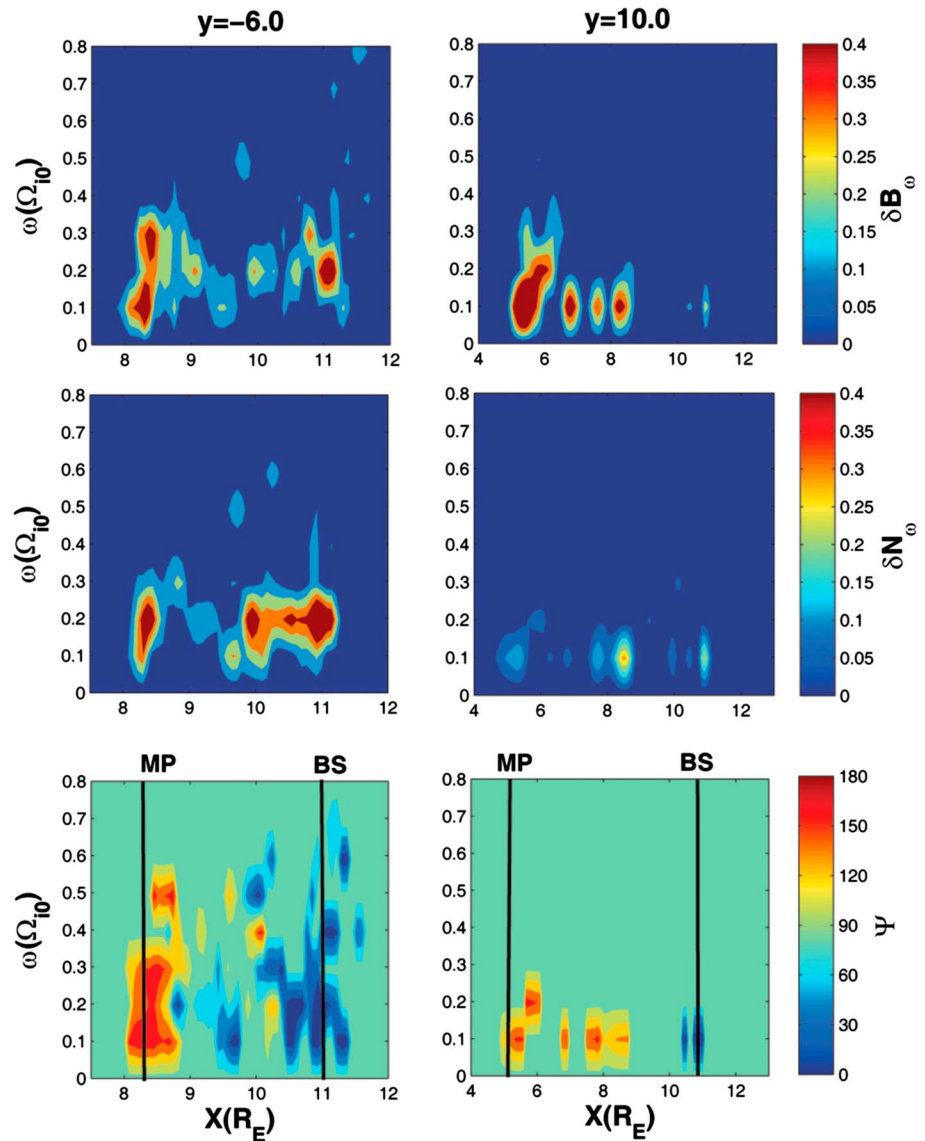
Figure 10. The power spectra of perturbations (first row) δB and (second row) δN in the ω-x space at (left column) $y = -6\,R_E$ and (right column) $y = 10\,R_E$ in the equatorial plane, respectively. (third row) The spectra of phase angle between δB and δN at the same locations, for Case 2.

Q-$\perp$ side at $y = 10\,R_E$, no in-phase waves are observed in the magnetosheath and magnetopause. Moreover, at $y = -6\,R_E$ on the Q-$\parallel$ shock side, the phase relation between B and N shows a general trend of abrupt change of wave modes from in-phase to antiphase near the magnetopause, whereas such phase transition is not seen at $y = 10\,R_E$ downstream of the Q-$\perp$ shock. Such a result, together with that shown in Figure 9, demonstrates the mode conversion process associated with the Q-$\parallel$ shock.

To illustrate the generation of KAWs as a consequence of the mode conversion process in the magnetopause, we now examine the wave structures in the magnetopause transition layer. The parallel wavelength of incoming waves on the magnetopause in our simulations is measured approximately to be 3–$8\,R_E$, with $\rho_i \sim 0.5d_{i0}$ locally, and the perpendicular wavelength to be roughly 0.2–$0.5\,R_E$. Around the subsolar region in the MPBL, Figure 11 shows the spatial profiles of B, N, $J_\parallel$, $E_\parallel$, and the magnetic field component B'_y, which is perpendicular to both the magnetopause normal ($\sim \boldsymbol{x}$) and the magnetic field, at $t = 88$ obtained in Case 2. For the average dominant $\omega \sim 0.3\Omega_{i0}$ as measured in the MPBL shown in Figure 10 due to mode conversion, the Alfvén resonance condition, $\omega = k_\parallel V_A(1 - \omega^2/\Omega_i^2) \sim k_\parallel V_A$, requires $V_A \sim 2.3V_{A0}$. This value of the Alfvén speed corresponds to $x \sim 9.9\,R_E$ as V_A ramps up quickly into the MPBL but maintains the resonance speed
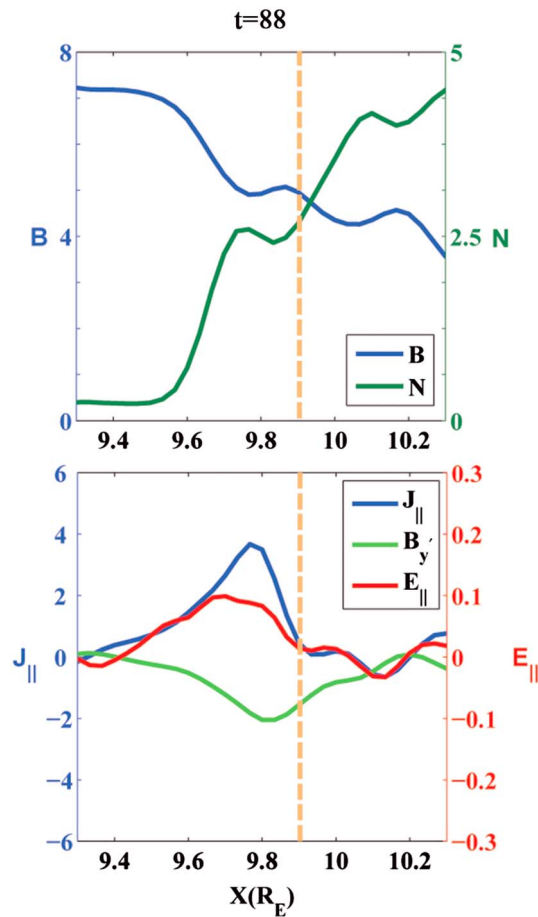
Figure 11. Spatial profiles of B, N, $J_\parallel$, $E_\parallel$, and B_y' (the magnetic field component perpendicular to both the magnetopause normal and the local magnetic field) at $t = 88$ around the subsolar region in the MPBL for Case 2. The vertical dashed lines mark the averaged resonance point.

near the predicted location in the transition layer, indicated by the orange vertical line in Figure 11. In the MPBL transition, where B increases and N decreases toward the magnetosphere, a strong local excitation of correlated $E_\parallel$, $J_\parallel$, and the transverse B_y' is observed, which confirms the existence of the predicted average Alfvén resonance point. Around this average location of the predicted Alfvén resonance point, $E_\parallel$ is strongly enhanced locally, and it then shows a purely decay spatial profile onto the magnetospheric side. Corresponding to the transverse magnetic perturbation, the magnetic field strength and density also change slightly, with an antiphase relation. This short wavelength structure with these well-correlated polarizations is a KAW that is excited at the Alfvén resonance surface due to mode conversion from compressional waves [*Hasegawa and Chen*, 1976], similar to Case 1. Also similar to the results of *Shi et al.* [2013], the waves are purely decayed into the magnetosphere.

Compared with Case 1 with the low $M_A = 3$, the excited KAWs appear to be confined in the MPBL. Based on the local theory and simulations of mode conversion, the excited KAWs are globally propagating modes with traveling direction reversed from that of the incident waves, radiating back to the region of the drivers [e.g., *Hasegawa and Chen*, 1976; *Johnson and Cheng*, 1997; *Lin et al.*, 2010, 2012] until being Landau damped. The conditions at the magnetopause, however, are more complicated. Due to the presence of the global antisunward convections in the magnetosheath, the mode-converted KAWs are subject to the influence of the magnetosheath flows and thus may be confined in the MPBL to form a standing wave pattern. As a result, the KAWs may be of eigenmode structures. Such effect is stronger in the cases with a supercritical Mach number. The existence of KAW eigenmodes in the MPBL and the magnetotail boundary layer has been suggested in connection with magnetic reconnection [*Dai*, 2009; *Dai et al.*, 2016].

The wave polarization relation shown in Figure 12, at $t = 120$, which is also nearly consistent with the theoretical lines in the circled region, $\delta E_x' \simeq \sqrt{1 + k_\perp^2 \rho_i^2} V_A \delta B_y' \simeq 1.1 V_A \delta B_y'$, where $\delta E_x'$ and $\delta B_y'$ are perpendicular to the magnetopause boundary normal, since the relation $k_\perp \rho_i \sim 0.5 - 1$ and $T_e/T_i \sim 0.1 - 0.2$ still holds here. The polarization properties are also similar to the ones shown in Case 1. Around the subsolar region at the magnetopause, it can be distinguished that two wave branches propagate northward and southward, separated around the equatorial plane, as expected and discussed in Case 1. In this case, the wave structures in the MPBL appear to be $k_y \rho_i \sim 0.5 - 1$ as well.

To see the longitudinal and latitudinal global structures associated with the mode conversion in Case 2 with the existence of B_y component in IMF, the poleward and duskward movements of KAWs, characterized by $E_\parallel$ due to mode conversion, are tracked and presented in Figure 13 with three snapshots from $t = 132$ to $t = 145$ for iso-surface of $|E_\parallel| = 0.13$. The speed and direction of the convective flow are shown by the scaled black arrows. In the cases of oblique (nonradial) IMF, the wave propagation velocity in the simulation (Earth) frame downstream of the shock is determined by the combination of the wave velocity in the plasma frame,
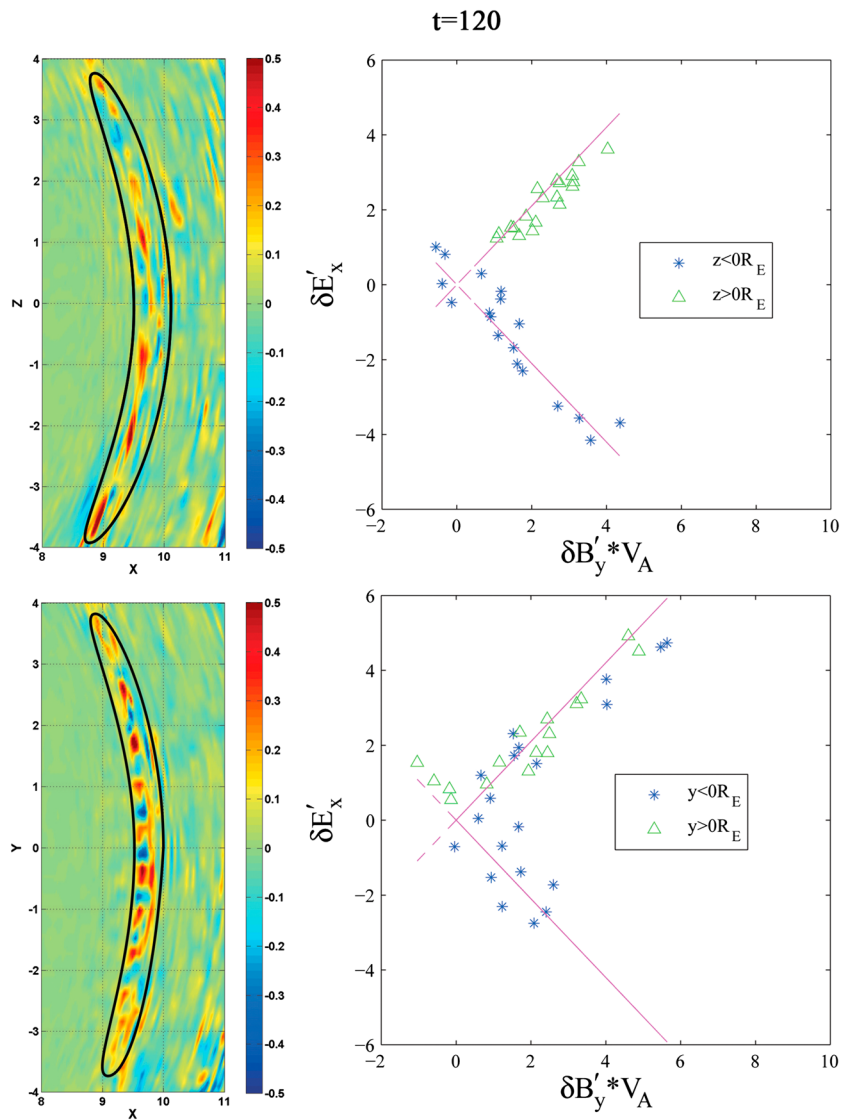
Figure 12. (top left) Spatial profile of $E_{\parallel}$ around the MPBL in the noon-meridian plane at $t = 120$ for Case 2. (top right) Corresponding polarization relation in the circled regions in Figure 12 (top left) showing Alfvén modes propagating in different directions along the field lines. (bottom left) Spatial profile of $E_{\parallel}$ around the MPBL in the equatorial plane at $t = 120$ for Case 2. (bottom right) Corresponding polarization relation in the circled regions in Figure 12 (bottom left) showing Alfvén modes. The violet dashed lines in Figure 12 (right column) represent the theoretically predicted polarization relation $\delta E'_x = \pm 1.1 V_A \delta B'_y$ for the KAWs.

which is nearly field aligned, and the convection velocity. As a result, as shown in Figure 5, it is seen that the subsolar region and dawnside (where the Q-$\parallel$ shock is centered) are abundant of compressional drivers in front of the magnetopause. Therefore, KAWs continuously form on the magnetopause not only on the dawnside but also extending through the subsolar area. They are seen to propagate along the field lines poleward to the cusp regions and carried away by the convective flows. Specifically, at $t = 132$, a group of KAW structures, shown in the left circle in Figure 13, is excited near the location where the convective flows are diverted tailward on the magnetopause as discussed in Figure 7. As time evolves, they are carried dawnward (duskward) for $y < -5 R_E$ ($y > -3 R_E$) by the convective flows. Because the KAWs also propagate along the field lines poleward, we see a much broader expansion poleward and tailward. In these snapshots it is shown that the KAWs from mode conversion can propagate from Q-$\parallel$ to Q-$\perp$ sides due to the duskward flows near the subsolar region. This can be seen from the traced KAWs around the subsolar region, shown in the right circle in each snapshot. For instance, at $t = 132$, the excited KAWs are seen in the subsolar region. At time $t = 138$, they propagate poleward and duskward but also bear decay because they are moving away
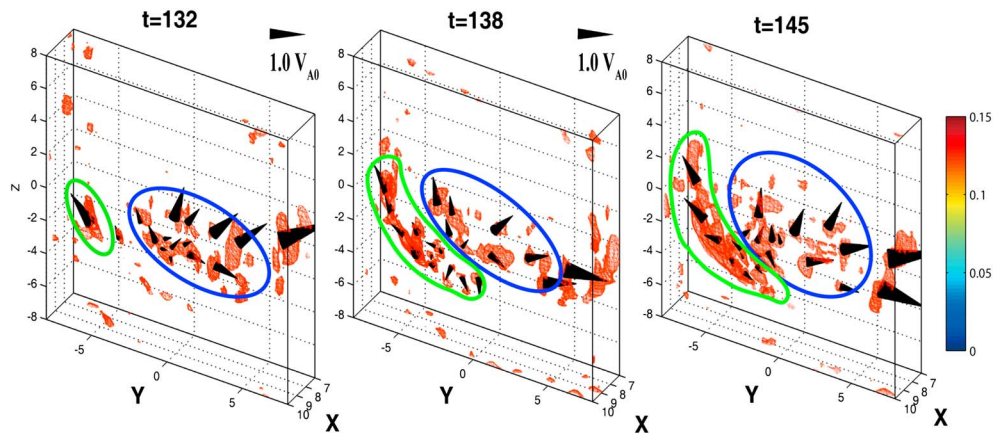
Figure 13. Isosurface plot of $|E_\parallel| = 0.13$ with tracked circles showing the same KAW structure generated around the magnetopause from $t = 132$ to $t = 145$ for Case 2. The black arrows show the convective flow direction and are scaled with the flow speed. Black reference arrows showing the normalized Alfvén speed are also given.

from the abundant source wave packet region. However, as the convective flows constantly carry compressive pulses down to this region, some local enhancements of KAWs are seen at later times. They may also merge with newly formed KAWs due to newly arrived compressional waves and be carried away by the convective flows. Note that due to the different flow convection speeds at various latitudes, the KAW packets expand along the north-south direction and may thus be weakened, so that their amplitudes appear to decrease as moving to higher latitudes, where their structures disappear from the isosurface of $|E_\parallel|$.

3.3. Simulation Results of the Case With IMF B_x, B_y, and B_z

For Case 3, with all nonzero components in IMF, the spatial contours of the magnetic field B with typical geo-space field lines and ion density N at $t = 90$, in the noon meridian and $z = -3\,R_E$ planes, are given in Figure 14. As expected, the self-generated bow shock and the magnetopause can be recognized around $13\,R_E$ and $10\,R_E$, respectively, in the subsolar region. In the existence of positive B_z component in IMF, the Q-∥ shock region is shifted to the south side on the bow shock, and since the IMF is more oblique (larger B_y component than Case 2), we see that the Q-∥ shock region is also shifted farther on the duskside for Case 3.

Similar to Case 2, for the oblique IMF case, compressional drivers are still found to reach the subsolar region of the magnetopause. Figure 15 shows spatial cuts of various quantities at $t = 66$ along the Sun-Earth and the $(x, 4.0, 4.0)\,R_E$ lines in the MPBL. In the subsolar MPBL (Figure 15, left column), the properties of the perturbations are quite similar to those discussed in Case 2. $E_\parallel$ and $J_\parallel$ are locally excited and well correlated. In short, these structures are still KAWs as identified in previous cases. However, at the locations
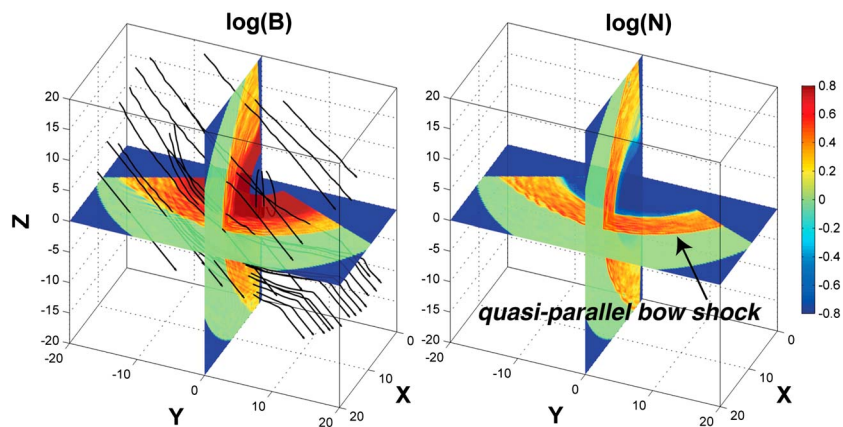

Figure 14. Spatial contours of B and N at $t = 90$ (in logarithmic scales) showing the 3-D structures of self-consistently generated bow shock and magnetopause, as well as the compressive pulses in the magnetosheath, for Case 3 in Table 1. Typical field lines are also shown in the magnetic field plot. The Q-∥ region is now located at the duskside and south side.
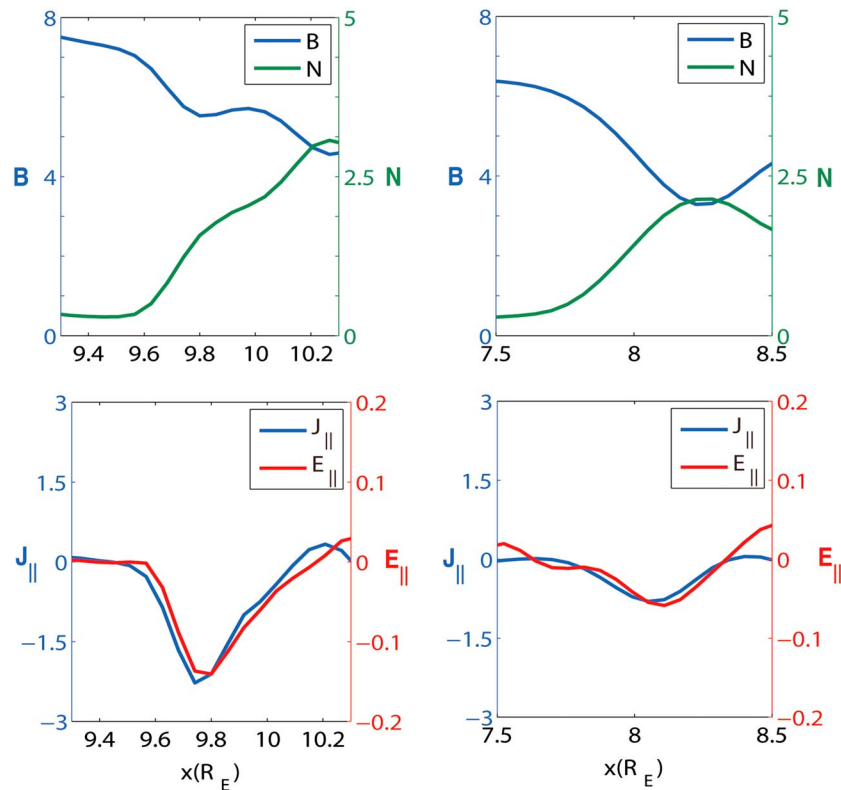
Figure 15. Spatial cuts of various quantities through the MPBL at $t = 66$ along two locations for Case 3: (left column) along the Sun-Earth line and (right column) along the $(x, 4.0, 4.0)$ R_E line.

(e.g., Figure 15, right column) away from the major mode conversion area, results are very different from those at subsolar: much weaker fluctuations of $E_\parallel$ and $J_\parallel$ (~50%), although they are still correlated. This may be because there is not much of compressional wave energy impact there. Also, there may be remnant of KAWs generated from the source region and carried by the convective flows.

The global KAW structures from the mode conversion in the existence of all IMF components are presented in Figure 16 for iso-surface of $|E_\parallel| = 0.1$ at $t = 91$ and $t = 95$, with scaled black arrows showing the convective flow direction and speed. At $t = 91$, three typical groups of KAW structures are excited and tracked around
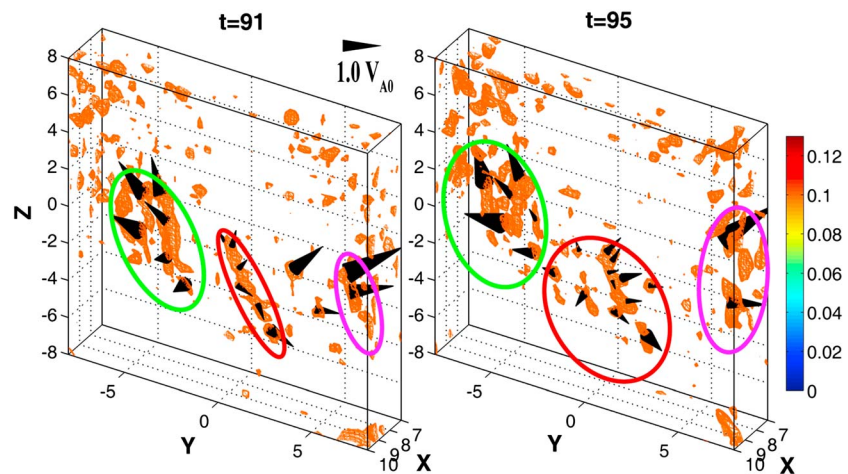

Figure 16. Isosurface plot of $|E_\parallel| = 0.1$ with tracked circles showing the same KAW structure generated around the magnetopause from $t = 91$ to $t = 95$ for Case 3. The black arrows show the convective flow direction and are scaled with the flow speed. A black reference arrow showing the normalized Alfvén speed is given.

the MPBL, shown by colored circles in Figure 16. At $t = 95$, they are seen to have similar behaviors: expand poleward and tailward and decay. The Q-∥ region is abundant of compressional drivers, which are carried earthward by the convective flows. These flows are diverted at $y \sim 0$ and $z \sim -2 \, R_E$ around the magnetopause. Consequently, the diverted northward and dawnward convection flows carrying compressional wave packets pass the subsolar magnetopause and even the downstream of the Q-⊥ shock. As discussed in Case 2, KAWs also propagate along the field lines. As a result, the main convection of the mode converted waves on the magnetopause is northward and dawnward, which can be seen from the green and red tracked circles in Figure 16. Also note that the "split" of the bottom wave structure in red circle is due to the convection flow diversion described above. On the duskside, the purple circle shows the tailward propagation of the waves to the dusk.

4. Summary

In summary, 3-D global hybrid simulations of mode conversion at the dayside magnetopause under various IMF conditions have been carried out and compared with the radial IMF case presented by *Shi et al.* [2013] in order to understand their influence on mode conversion. In addition, a case under a smaller Mach number and radial IMF is also discussed and compared with that of *Shi et al.* [2013] in order to understand the effects of the Mach number. Three-dimensional broadband structures of KAWs are found to be generated by the interaction between foreshock compressional waves from the Q-∥ shock and the magnetopause. The global propagation and evolution of the waves are presented. The main results can be summarized as follows.

1. The mode conversion to KAWs is found around in the MPBL for the case of radial IMF with a near-critical Mach number ($M_A = 3$). Although the $J_\parallel$ and $E_\parallel$ associated with the excited KAWs are weaker than those in the supercritical cases with $M_A = 5$ [*Shi et al.*, 2013], significant laminar k_x modes of KAWs are present in the MPBL around the subsolar area downstream of the Q-∥ shock. Compared with the case with a supercritical Mach number, the MPBL itself becomes broadened. A much broader mode conversion region inside the MPBL has also been observed. The resulting KAWs can be carried to the regions downstream of the Q-⊥ shock as well due to the existence of azimuthal component of flow convection at the mode conversion location.

2. Due to the presence of the antisunward convections in the magnetosheath, the mode-converted KAWs are subject to the influence of the magnetosheath flows and thus may be confined in the MPBL. As a result, the KAWs appear to be of eigenmode structures with a nominal $k_x \rho_i \sim 0.5 - 1$. Such effect is stronger in the cases with a supercritical Mach number with $M_A = 5$. Further theoretical studies are needed to understand the KAW structures at the magnetopause in the presence of various magnetosheath flows.

3. For cases under an oblique IMF with a finite B_y, the amplitude of magnetosheath compressional waves is found to be larger at the Q-∥ shock than at the Q-⊥ shock. Downstream of the Q-∥ shock, wave perturbations changes from an in-phase relation between B and N in the magnetosheath to an antiphase relation near the MPBL. Downstream of the Q-⊥ shock, however, an antiphase relation between B and N is dominant throughout the magnetosheath and magnetopause except near the shock transition.

4. For cases under an oblique IMF with a finite B_y, the compressional drivers are found to reach an extended region including the subsolar region of the magnetopause due to the combined effects of wave propagation in the plasma frame and flow convection. Therefore, mode conversion process associated with the compressional waves of the Q-∥ shock takes place in a broad dawn-dusk and south-north region in the MPBL.

5. In cases of $B_z > 0$ in IMF in GSM system, the KAW structures are overall more intense in the Southern (Northern) Hemisphere with $B_x > 0$ ($B_x < 0$) in IMF.

6. The structure, propagation, and time evolution of KAWs, with $k_\perp \rho_i \sim 0.5 - 1$ and satisfying with the Alfvén resonance condition $\omega \simeq k_\parallel V_A$, from mode conversion in the 3-D magnetopause are identified and presented. The KAW perturbations move obliquely around the MPBL, propagating poleward and carried away azimuthally by the convection plasma flows.

References

Anderson, R. R., C. C. Harvey, M. M. Hoppe, and B. T. Tsurutani (1982), Plasma waves near the magnetopause, *J. Geophys. Res.*, *87*, 2087–2107.
Bellan, P. M. (2012), Improved basis set for low frequency plasma waves, *J. Geophys. Res.*, *117*, A12219, doi:10.1029/2012JA017856.
Blanco-Cano, X., N. Omidi, and C. Russell (2006), ULF waves and their influence on bow shock and magnetosheath structures, *Adv. Space Res.*, *37*(8), 1522–1531, doi:10.1016/j.asr.2005.10.043.

Blanco-Cano, X., N. Omidi, and C. T. Russell (2009), Global hybrid simulations: Foreshock waves and cavitons under radial interplanetary magnetic field geometry, *J. Geophys. Res.*, *114*, A01216, doi:10.1029/2008JA013406.

Chaston, C., et al. (2008), Turbulent heating and cross-field transport near the magnetopause from THEMIS, *Geophys. Res. Lett.*, *35*, L17S08, doi:10.1029/2008GL033601.

Chaston, C. C., M. Wilber, F. S. Mozer, M. Fujimoto, M. L. Goldstein, M. Acuna, H. Reme, and A. Fazakerley (2007), Mode conversion and anomalous transport in Kelvin-Helmholtz vortices and kinetic Alfvén waves at the Earth's magnetopause, *Phys. Rev. Lett.*, *99*(17), 175004, doi:10.1103/PhysRevLett.99.175004.

Chaston, C. C., et al. (2005), Energy deposition by Alfvén waves into the dayside auroral oval: Cluster and fast observations, *J. Geophys. Res.*, *110*, A02211, doi:10.1029/2004JA010483.

Czaykowska, A., T. M. Bauer, R. A. Treumann, and W. Baumjohann (1998), Mirror waves downstream of the quasi-perpendicular, *J. Geophys. Res.*, *103*(A3), 4747–4753, doi:10.1029/97JA03245.

Dai, L. (2009), Collisionless magnetic reconnection via Alfvén eigenmodes, *Phys. Rev. Lett.*, *102*(24), 245003, doi:10.1103/PhysRevLett.102.245003.

Dai, L., C. Wang, Y. Zhang, B. Lavraud, J. Burch, C. Pollock, and R. B. Torbert (2016), Kinetic Alfvén wave explanation of the Hall fields in magnetic reconnection, *Geophys. Res. Lett.*, *44*, 634–640, doi:10.1002/2016GL071044.

Eastwood, J. P., E. A. Lucek, C. Mazelle, K. Meziane, Y. Narita, J. Pickett, and R. A. Treumann (2005), The foreshock, *Space Sci. Rev.*, *118*(1–4), 41–94, doi:10.1007/s11214-005-3824-3.

Fairfield, D. H., W. Baumjohann, G. Paschmann, H. Lühr, and D. G. Sibeck (1990), Upstream pressure variations associated with the bow shock and their effects on the magnetosphere, *J. Geophys. Res.*, *95*(A4), 3773–3786, doi:10.1029/JA095iA04p03773.

Farris, M. H., C. T. Russel, R. J. Fitzenreiter, and K. W. Ogilvie (1994), The subcritical, quasi-parallel, switch-on shock, *Geophys. Res. Lett.*, *21*, 837–840, doi:10.1029/94GL00697.

Fujimoto, M., T. Terasawa, T. Mukai, Y. Saito, T. Yamamoto, and S. Kokubun (1998), Plasma entry from the flanks of the near-Earth magnetotail, *J. Geophys. Res.*, *103*, 4391–4408.

Fuselier, S. A., K. J. Trattner, and S. M. Petrinec (2000), Cusp observations of high- and low-latitude reconnection for northward interplanetary magnetic field, *J. Geophys. Res.*, *105*, 253–266, doi:10.1029/1999JA900422.

Gosling, J. T., M. F. Thomsen, S. J. Bame, W. C. Feldman, and N. Sckopke (1982), Evidence for specularly reflected ions upstream from the quasi-parallel bow shock, *Geophys. Res. Lett.*, *9*(12), 1333–1336, doi:10.1029/GL009i012p01333.

Hasegawa, A., and L. Chen (1976), Kinetic processes in plasma heating by resonant mode conversion of Alfvén wave, *Phys. Fluids*, *19*, 1924–1934.

Hasegawa, H., K. Maezawa, T. Mukai, and Y. Saito (2002), Plasma entry across the distant tail magnetopause 2. Comparison between MHD theory and observation, *J. Geophys. Res.*, *107*(A6), 1073, doi:10.1029/2001JA900138.

Hasegawa, H., M. Fujimoto, K. Maezawa, Y. Saito, and T. Mukai (2003), Geotail observations of the dayside outer boundary region: Interplanetary magnetic field control and dawn-dusk asymmetry, *J. Geophys. Res.*, *108*, 1163, doi:10.1029/2002JA009667.

Johnson, J. R., and C. Z. Cheng (1997), Kinetic Alfvén waves and plasma transport at the magnetopause, *Geophys. Res. Lett.*, *24*(11), 1423–1426, doi:10.1029/97GL01333.

Johnson, J. R., C. Z. Cheng, and P. Song (2001), Signatures of mode conversion and kinetic Alfvén waves at the magnetopause, *Geophys. Res. Lett.*, *28*(2), 227–230, doi:10.1029/2000GL012048.

Kajdic, P., X. Blanco-Cano, N. Omidi, K. Meziane, C. T. Russell, J. A. Sauvaud, I. Dandouras, and B. Lavraud (2013), Statistical study of foreshock cavitons, *Ann. Geophys.*, *31*, 2163–2178, doi:10.5194/angeo-31-2163-2013.

Karimabadi, H., et al. (2014), The link between shocks, turbulence, and magnetic reconnection in collisionless plasmas, *Phys. Plasmas*, *21*(6), 062308.

Lin, Y. (2003), Global-scale simulation of foreshock structures at the quasi-parallel bow shock, *J. Geophys. Res.*, *108*(A11), 1390, doi:10.1029/2003JA009991.

Lin, Y., and X. Y. Wang (2005), Three-dimensional global hybrid simulation of dayside dynamics associated with the quasi-parallel bow shock, *J. Geophys. Res.*, *110*, A12216, doi:10.1029/2005JA011243.

Lin, Y., X. Y. Wang, and S.-W. Chang (2007), Connection between bow shock and cusp energetic ions, *Geophys. Res. Lett.*, *34*, L11107, doi:10.1029/2007GL030038.

Lin, Y., J. R. Johnson, and X. Y. Wang (2010), Hybrid simulation of mode conversion at the magnetopause, *J. Geophys. Res.*, *115*, A04208, doi:10.1029/2009JA014524.

Lin, Y., J. R. Johnson, and X. Y. Wang (2012), Three-dimensional mode conversion associated with kinetic Alfvén waves, *Phys. Rev. Lett.*, *109*, 125003, doi:10.1103/PhysRevLett.109.125003.

Nishino, M. N., M. Fujimoto, T.-D. Phan, T. Mukai, Y. Saito, M. M. Kuznetsova, and L. Rastätter (2008), Anomalous flow deflection at earth's low-Alfvén-Mach-number bow shock, *Phys. Rev. Lett.*, *101*(6), 065003.

Omidi, N., K. B. Quest, and D. Winske (1990), Low Mach number parallel and quasi-parallel shocks, *J. Geophys. Res.*, *95*, 20,717–20,730, doi:10.1029/JA095iA12p20717.

Phan, T. D., and G. Paschmann (1996), Low-latitude dayside magnetopause and boundary layer for high magnetic shear 1. Structure and motion, *J. Geophys. Res.*, *101*, 7801–7816, doi:10.1029/95JA03752.

Phan, T. D., R. P. Lin, S. A. Fuselier, and M. Fujimoto (2000), Wind observations of mixed magnetosheath-plasma sheet ions deep inside the magnetosphere, *J. Geophys. Res.*, *105*, 5497–5506.

Pi, G., J.-H. Shue, K. Grygorov, H.-M. Li, Z. Němeček, J. Šafránková, Y.-H. Yang, and K. Wang (2017), Evolution of the magnetic field structure outside the magnetopause under radial IMF conditions, *J. Geophys. Res. Space Physics*, *122*, 4051–4063, doi:10.1002/2015JA021809.

Price, C. P., D. W. Swift, and L.-C. Lee (1986), Numerical simulation of nonoscillatory mirror waves at the Earth's magnetosheath, *J. Geophys. Res.*, *91*(A1), 101–112, doi:10.1029/JA091iA01p00101.

Rezeau, L., A. Morane, S. Perraut, A. Roux, and R. Schmidt (1989), Characterization of Alfvenic fluctuations in the magnetopause boundary layer, *J. Geophys. Res.*, *94*, 101–110.

Russell, C. T., and R. C. Elphic (1978), Initial ISEE magnetometer results: Magnetopause observations, *Space Sci. Rev.*, *22*, 681–715, doi:10.1007/BF00212619.

Russell, C. T., and R. C. Elphic (1979), ISEE observations of flux transfer events at the dayside magnetopause, *Geophys. Res. Lett.*, *6*, 33–36, doi:10.1029/GL006i001p00033.

Shi, F., Y. Lin, and X. Wang (2013), Global hybrid simulation of mode conversion at the dayside magnetopause, *J. Geophys. Res. Space Physics*, *118*, 6176–6187, doi:10.1002/jgra.50587.

Sibeck, D. G., et al. (1989), The magnetospheric response to 8-minute period strong-amplitude upstream pressure variations, *J. Geophys. Res.*, *94*(A3), 2505–2519, doi:10.1029/JA094iA03p02505.

Stasiewicz, K., C. E. Seyler, F. S. Mozer, G. Gustafsson, J. Pickett, and B. Popielawska (2001), Magnetic bubbles and kinetic Alfvén waves in the high-latitude magnetopause boundary, *J. Geophys. Res.*, *106*(A12), 29,503–29,514, doi:10.1029/2001JA900055.

Swift, D. W. (1996), Use of a hybrid code for a global-scale plasma simulation, *J. Comput. Phys.*, *126*, 109–121.

Tang, B., C. Wang, and W. Li (2013), The magnetosphere under the radial interplanetary magnetic field: A numerical study, *J. Geophys. Res. Space Physics*, *118*, 7674–7682, doi:10.1002/2013JA019155.

Thomsen, M. F., J. T. Gosling, T. G. Onsager, and C. T. Russel (1993), Ion and electron heating at the low-Mach-number quasi-parallel bow shock, *J. Geophys. Res.*, *98*, 3875–3888, doi:10.1029/92JA02560.

Tsurutani, B. T., and R. G. Stone (1985), *Collisionless Shocks in the Heliosphere: Reviews of Current Research*, 303 pp., AGU, Washington, D. C.

Tsurutani, B. T., and R. M. Thorne (1982), Diffusion processes in the magnetopause boundary layer, *Geophys. Res. Lett.*, *9*, 1247–1250, doi:10.1029/GL009i011p01247.

Turner, D., N. Omidi, D. G. Sibeck, and V. Angelopoulos (2013), First observations of foreshock bubbles upstream of Earth's bow shock: Characteristics and comparisons to HFAs, *J. Geophys. Res. Space Physics*, *118*, 1552–1570, doi:10.1002/jgra.50198.

Wang, X. Y., and Y. Lin (2003), Generation of nonlinear Alfvén and magnetosonic waves by beam–plasma interaction, *Phys. Plasmas*, *10*(9), 3528–3538, doi:10.1063/1.1599359.

Wang, X. Y., Y. Lin, and S.-W. Chang (2009), Hybrid simulation of foreshock waves and ion spectra and their linkage to cusp energetic ions, *J. Geophys. Res.*, *114*, A06203, doi:10.1029/2008JA013745.

Wibberenz, G., F. Zöllich, H. M. Fischer, and E. Keppler (1985), Dynamics of intense upstream ion events, *J. Geophys. Res.*, *90*(A1), 283–301, doi:10.1029/JA090iA01p00283.

Wing, S., and J. R. Johnson (2009), Substorm entropies, *J. Geophys. Res.*, *114*, A00D07, doi:10.1029/2008JA013989.

Yang, Z., C. Huang, Y. D. Liu, G. K. Parks, R. Wang, Q. Lu, and H. Hu (2016), Global explicit particle-in-cell simulations of the nonstationary bow shock and magnetosphere, *Astrophys. J. Suppl. Ser.*, *225*(1), 13.

Yao, Y., C. C. Chaston, K. Glassmeier, and V. Angelopoulos (2011), Electromagnetic waves on ion gyro-radii scales across the magnetopause, *Geophys. Res. Lett.*, *38*, L09102, doi:10.1029/2011GL047328.